Simulated and experimental study of laser-beam-induced thermal aberrations in precision optical systems

Hua Chen,* Huaijiang Yang, Xinfeng Yu, and Zhenguang Shi

State Key Laboratory of Applied Optics, Changchun Institute of Optics, Fine Mechanics
and Physics, Chinese Academy of Science, Changchun 130033, China

*Corresponding author: chenhua.tyb@126.com

Received 15 March 2013; revised 22 May 2013; accepted 23 May 2013;
posted 23 May 2013 (Doc. ID 187142); published 19 June 2013

Precision optical systems that utilize laser beams as working media usually suffer from thermal aberrations caused by absorbed energy. Based on a specially designed three-lens system, the causes and contributions of mechanical structures to the system's thermal aberrations are studied. The contribution of three thermal effects, surface deformation, change of refractive index, and stress birefringence on the system's thermal aberrations, is analyzed respectively through an integrated optomechanical simulation method. The impact of the structure's thermal dissipating capability and structure configuration on the system's thermal aberrations is analyzed, too. Experiments have been carried out to validate the correctness and accuracy of the simulation method. Both the simulated and tested results can provide a reference for structure design and thermal aberration analysis of the similar optical systems. © 2013 Optical Society of America

OCIS codes: (120.6650) Surface measurements, figure; (120.6810) Thermal effects; (220.1000) Aberration compensation; (220.3740) Lithography; (120.4880) Optomechanics; (120.3940) Metrology.

http://dx.doi.org/10.1364/AO.52.004370

1. Introduction

Precision optical systems such as optical lithographical projection lenses utilize laser beams as working media. The transmitted laser energy, though as low as a few watts, will cause unwanted thermal aberrations [1–3], and the nonuniform distribution of energy, for example, under dipole illumination conditions, makes it worse and more complicated [4,5]. Previous studies attributed thermal aberrations to three temperature effects: thermal deformation of lens surface, change of refractive index, and stress-birefringence [6]. A few design rules or athermal methods have been developed, including choosing compatible thermal expansion coefficients materials of the optical element and its mount to reduce expansion deformation of optical surfaces and thermal stresses, choosing dimensions and materials to counteract the defocus effect, and designing kinematic supports to reduce thermal stress in the metal–glass interfaces [6–8]. These rules or methods are very important during the design process of optical systems, which work in a large range of temperatures and the temperature shifts with the whole system. The main concern is the thermal defocus effect [9], such as done by aerial cameras.

Optical lithographical projection lenses, however, have some differences. First, to accomplish high image performance, the surface figure of most of the 20 s optical elements are better than 1 nm rms [10]. The first concern of mechanical designers is to introduce as little figure change as possible no matter if it's in cold or heated conditions. Second, under working conditions, the projection lens is heated by absorbed laser energy, leading to temperature gradients in the whole system, the characteristics

---

1559-128X/13/184370-07$15.00/0

of which are hot on the inside, cold on the outside. The distributions of temperature in optical lenses are highly dependent on the illumination pattern that in general is nonuniform, inducing asymmetric thermal aberrations. The defocus effect, however, is not a big concern because it can be compensated by shift of optical elements [11]. The main concern to the mechanical designer is how to reduce these asymmetric thermal aberrations to an acceptable level without utilizing active deformable lens or other complicated compensation methods.

Because of a lack of guidance or experiences for the design of such kinds of optical systems, we faithfully believe that utilization of low thermal expansion coefficient metal as supporting a structure's material is the best way to protect the surface figure from degeneration and to reduce thermal stresses. And whenever the system's thermal aberration overruns the expectation, we should improve the design of supporting structures, especially to improve their capability of dissipating heat. These requirements make the mechanical designers confused because low thermal expansion coefficient metals generally have low thermal conductive coefficients and increasing thermal dissipating capability always means higher thermal conductivity and heavier structure masses.

To resolve the abovementioned problems, in this paper we first studied the contribution of each of the three thermal effects: surface deformation, refractive index change, and stress-birefringence to the system thermal aberrations through an integrated opto-mechanical analysis method; then we studied the impact of different structure thermal dissipating capabilities and special structure configuration on system thermal aberrations. A specially designed experimental system consisting of three transmissive lenses was built up and experiments were carried out to validate the analysis results.

2. Setup of the Experimental System

The experimental system consists of three transmissive lenses. Two circular film electrical heaters are affixed to the up surface of each lens as heating sources to simulate the absorbed laser energy. To reduce the influence of the environmental temperature fluctuations to the system, a constant temperature water jacket is set on the periphery of the system with a gap of 0.8 mm, and the temperature of circulated water is set to 22°C, the stability of which is controlled better than ±0.01°C over a 72 h range. The system is installed on a Zygo 12 in. vertical interferometer to test its wavefront, as Fig. 1 shows.

The three lenses are made of fused silica; the mechanical structures are made of metal 304. The first and the third lens are mounted with the retaining ring method and the lens-to-mount interface is tangential. This kind of support provides a uniform thermal conduction path around the lens. The second lens is mounted with three point kinematic mounts, which introduce the least thermal stress and constraint to the lens when heated. The shortcoming is that the thermal conduction path is unsymmetrical. The water jacket is a 2 mm thick Al alloy tube with the same profile of the lens house, and the water pipe is welded around its outside surfaces.

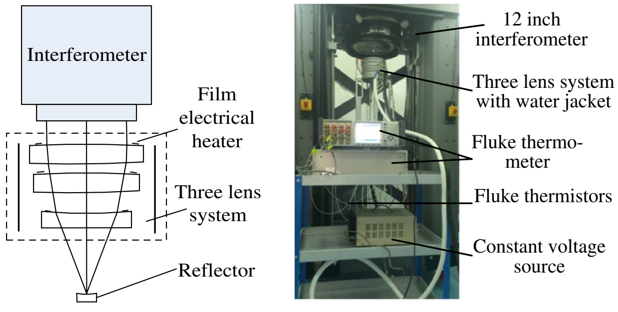

(a) (b)

Fig. 1. Setup of the three lens experimental system. (a) Diameter of the three lenses is between 125 and 152 mm, thickness is about 36 mm, the diameter of the six electrical film heaters is 20 mm, resistance is 31 Ω, thickness is 0.2 mm. (b) Photograph of the experimental system.

In total, 13 high precision thermistor temperature sensors are arranged in and outside the experimental system to monitor changes of temperature with time. As Fig. 2 shows, each three thermistors were stuck on one lens. Because the sensor is very tiny, 1.5 mm in diameter, it is convenient to use.

3. Contribution of the Three Thermal Effects to System Thermal Aberrations

The integrated optomechanical analysis method is used to estimate the system's thermal aberrations [12]. After the system's geometry model is finished, a FEM model is built up in the NX Advanced Simulation software that is used to generate temperature distribution results and then use these results as the structure's temperature load to generate the system's thermal deformation and thermal stress results. The temperature, displacement, and stress results are processed, respectively, by SigFit (SigFit is a trademark of Sigmadyne, Inc.), an interface software to generate surface figure or wavefront data readable by optical analysis tools; then we use Code V (Code V is a trademark of Synopsys, Inc.) software to analyze the system's thermal aberrations.

The FEM model of the system includes 336,499 elements and 164,199 nodes. The input voltage of each film electrical heater is set to 1 V, according to the power function; that is, $P = U^2/R = 0.0323$ watt. This power is close to the maximum absorbed

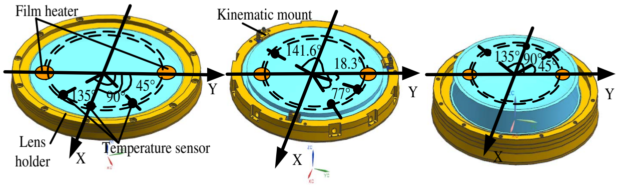

(a) (b) (c)

Fig. 2. Arrangement of the temperature sensors and film electrical heaters on the three lenses.

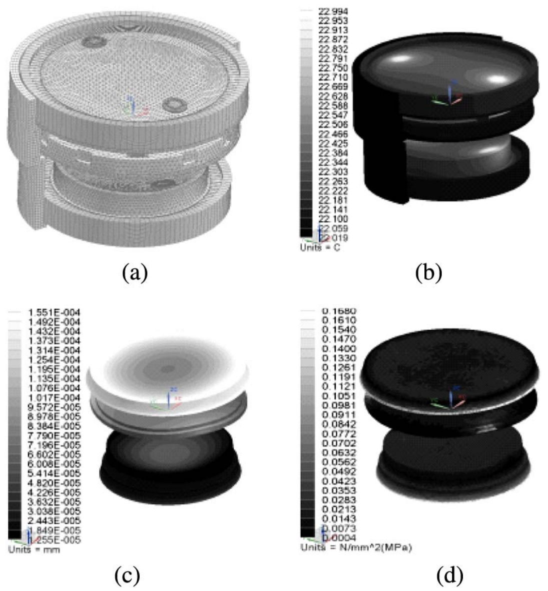

Fig. 3. (a) FEM model of the three-lens system. (b) Temperature distribution of the system. (c), (d) Displacement and stress distribution of lens nodes when use temperature results in (b) as temperature load.

laser energy by one hot spot of the lithographical lens when it is illustrated by dipole illumination. Figure 3 shows the model and a set of results.

A. Evaluation of the Surface Deformation-Induced Thermal Aberrations

The surface displacement result at each node exported by NX Nastran includes six components: dx, dy, dz, $d\theta_x$, $d\theta_y$, and $d\theta_z$. With these displacement components we can calculate the six rigid body motion components, T_x, T_y, T_z, R_x, R_y, and R_z of the deformed surface, which are the three translation components along coordinate axes and three rotation components about coordinate axes. Subtractions of rigid body motions are then done to derive new nodal displacement results and Code V standard Zernike polynomials are used to fit the new displacement results [13]. The polynomial coefficients for each surface are then imported to Code V as interferogram perturbance; analysis is done to generate the surface deformation-induced thermal aberration that is also described by Code V standard Zernike polynomial coefficients. Figure 4 is the PV, the rms values of the six surfaces, and the system aberration result. The maximum surface change is 1.44 nm rms and the induced system aberration is 0.67 nm rms.

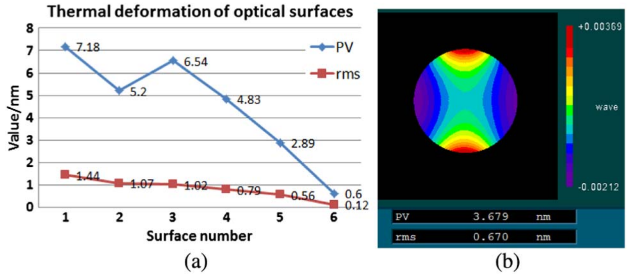

Fig. 4. Simulated results. (a) PV and rms values of the six surfaces (without power) and (b) system thermal aberration induced by surface deformations.

B. Evaluation of Change of Refractive Index-Induced Thermal Aberrations

When thermal analysis is done, we can get the discrete nodal temperature of the lens. Optical path integration is operated between the entrance surface and the exit surface of each lens. The integration paths originate from the finite element nodes of the entrance surface with paths proportional to the apertures of the entrance and exit surfaces, as Fig. 5 shows. The number of integration intervals is defined along each path, and optical path difference (OPD) due to temperature variations at the integration points is computed according to the following equations [13]:

$$\mathrm{OPD} = -\sum_{i=1}^{N} \delta n_i \delta l_i, \quad \delta n_i = \int_{T_0}^{T_i} k \mathrm{d}T. \tag{1}$$

In the equation, N is the number of integration intervals along the optical path, δn_i is the change of refractive index of the ith integration point, δl_i is the path length associated with the ith integration point, and k is the temperature coefficient of the refratctive index of lens material.

An OPD map is then produced for each lens and is subsequently fit to Code V standard Zernike polynomials. The polynomial coefficients are imported into CODE V as wavefront interferogram perturbance and analysis is done to generate the change of refractive index induced thermal aberrations. Figure 6 is the PV, rms values of the three-lens wavefront, and system aberration result. The maximum wavefront change is 9.56 nm rms and the induced system aberration is 22.23 nm rms.

C. Evaluation of Stress Birefringence Effects

As shown in Fig. 3, because of nonuniform distributed temperature in lens and constraint of thermal expansion, there are nonuniform distributed stresses in the three lenses. Apart from the edge effect-caused stress centralization, which is inaccurate in most FEM simulations, the maximum value of stress in the x–y plane is less than 0.03 MPa in the three lenses, and the maximum stress difference is less than 0.006 MPa.

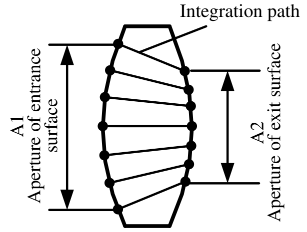

Fig. 5. Definition of integration paths for OPD analysis.

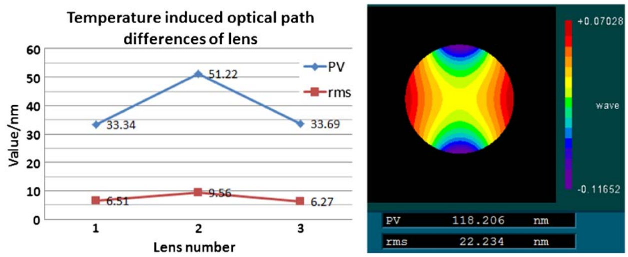

(a) (b)

Fig. 6. Simulated results. (a) PV and rms wavefront values of the three lenses and (b) system thermal aberration induced by change of refractive index.

Optical isotropic glass becomes anisotropic through mechanical and thermal induced stress, i.e., the refractive index in the glass becomes anisotropic. There are two stress optical coefficients related to the stress birefringence of fused silica, q_{11} and q_{12}, which have the following relationship with birefringence:

$$\text{Birefringence} = R \bullet (\sigma_x - \sigma_y),$$
$$R = \frac{1}{2} \bullet n_0^3 \bullet (q_{11} - q_{12}), \tag{2}$$

where R is the stress coefficient for the material with a unit of nm/cm/MPa, n_0 is the refractive index of the isotropic material, and σ_x and σ_y are the stress along the two orthogonal axes in a plane perpendicular to the beam path axis. As reference, the R value of Corning's fused silica is 35 nm/cm/MPa at 633 nm [14]. According to Eq. (2), the maximum birefringence caused by thermal stress is less than 0.21 nm/cm, far lower than the material's initial birefringence after manufacture; hence it is not a concern in this system.

As a reference, the effect of refractive index change due to thermal stress is estimated with the average change in OPD, which is called the stress-optic effect. It is accomplished by integration of optical path defined in Section 3.B. according to the following Eq. [13]:

$$\text{OPD}_{\text{stress}} = -\sum_{i=1}^{N} \left(\frac{\Delta n_1 + \Delta n_2}{2} \right)_i \delta l_i. \tag{3}$$

In the equation, Δn_1 and Δn_2 are the refractive index change along the two orthogonal axes in a plane perpendicular to the beam path axis. Both of them are related to the stress components via stress optical coefficients q_{11} and q_{12}, and the calculation methods have been elaborated in the literature [15,16]. Utilizing Schroeder measured values [17] for p_{11} and p_{12} at wavelength of 632.8 nm and the Young's modulus and Poisson ratio of Corning's fused silica, the values of q_{11} and q_{12} can be derived, which are 0.5659e−6/MPa and 2.857e−6/MPa, respectively. The average changes in OPD of the three lenses are 0.017, 0.036, and 0.035 nm rms respectively; hence the stress effects are negligible in this system.

D. Discussion and Experimental Validation of the Analysis

The simulated results shown in 3(a), 3(b), and 3(c) illustrate that the system's thermal aberration is mainly caused by temperature gradient-induced refractive index change. Though the surface figure change of three surfaces overruns 1 nm rms, the combined thermal effect of the six surfaces' deformation is only about 1/33 of the effect of the change of refractive index. This suggests that reduction of surface deformation is less important relative to reduction of temperature gradients when we conduct the system's structure design. Small temperature change such as 1°C will induce neglectable amount of birefringence. A further analysis that combines the surface deformation and change of refractive index effects shows that the total system thermal aberration is 21.57 nm rms.

The experiment is carried out to make a direct measurement of the system's thermal aberration:

1. Install the system on the vertical interferometer, start the circulated water temperature control system, and the thermometer;
2. Measure the wavefront when the temperature of the system reaches thermal balance;
3. Start the constant voltage source, set the voltage to 1 V;
4. Repeat step 2.

The system's thermal wavefront aberration can be calculated by subtracting the result in step 2 from the result in step 4. In this way, there is no interferometer system error in the tested thermal aberration results because it was wiped off by subtraction. The rms repeatability of the wavefront measurement is about ±0.1 nm rms (1σ). The system takes about 6 h to reach thermal balance. Because of air turbulence and long term mechanical drifts, the repeatability of the thermal aberration results is about ±0.11 nm rms (1σ).

Figure 7 shows a group of the tested results; the system's transmissive wavefront before being heated is about 9.56 nm rms, and when it is heated and reaches thermal balance, the transmissive wavefront degenerates to 22.26 nm rms; the total thermal aberration is about 19.36 nm rms, as shown in Fig. 7(c). Figure 7(d) is a figure plot of the Code V Zernike coefficients of the thermal aberration. Figures 7(e) and 7(f) are the residual of Zernike polynomials fitting, from which we can find that the fitting is effective because the residual is mainly high frequency components.

It is common that there is an azimuthal difference between the tested and the simulated results, and it can be eliminated by rotation of the tested results about the center of the data. The rotation angle is defined by the centerlines crossing the centers of the two circle electrical film heaters of the tested and simulated system. Figure 8 is a comparison of the Z4 ~ Z45 Code V standard Zernike coefficients of the tested and simulated results after data alignment. Comparing Figs. 8(a) and 7(d), we can find that

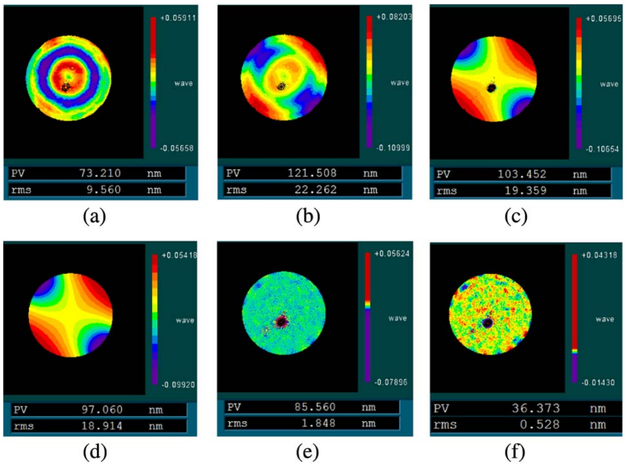

(a) (b) (c)

(d) (e) (f)

Fig. 7. Experimental results. (a) System wavefront before heated, (b) system wavefront after heated, (c) system thermal aberration calculated by subtraction of interferogram, (d) Code V standard Zernike fitting of (c), (e) residual of Zernike polynomials fitting, and (f) FFT low pass filter of (e), and the cutoff period is 4 mm.

rotation of data will introduce error to the results, but the magnitude is negligible. The error introduced by the tiny rotation error is also negligible [18]. The main components of the thermal aberrations are astigmatism, tetrad-foil, hexafoil, and a little amount of trefoil; the rest of the aberration components are too small to be considered. The difference between the tested and simulated results is about 2.78 nm rms and is mostly astigmatism aberration (which is caused mainly by the heat loss of the film heater in the experiment), as shown in Fig. 8(c), which is very small compared to the total 18.83 nm rms thermal aberrations.

Figure 9 is the comparison of the tested and simulated lens temperature. Thermal boundary conditions, such as thermal contact resistance, air gap thermal convection coefficients between the water jacket and the lens tube, and the error of the temperature tests, have been confirmed through specifically designed experiments to make the simulation credible. From the comparison we can find that the simulated results are very close to the tested results both with temperature and thermal aberrations, proving the correctness and accuracy of the simulation.

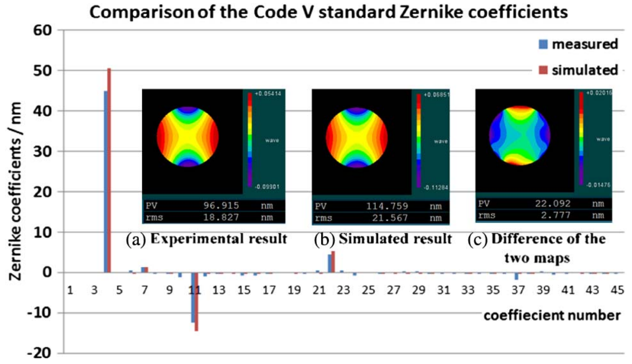

Fig. 8. Z4 ~ Z45 Code V standard Zernike coefficients of the tested and simulated thermal aberrations. (a) Experimental result after data alignment, (b) simulated result combining both surface deformation and OPD effects, and (c) figure generated from corresponding Zernike term coefficient subtraction of (a) and (b).

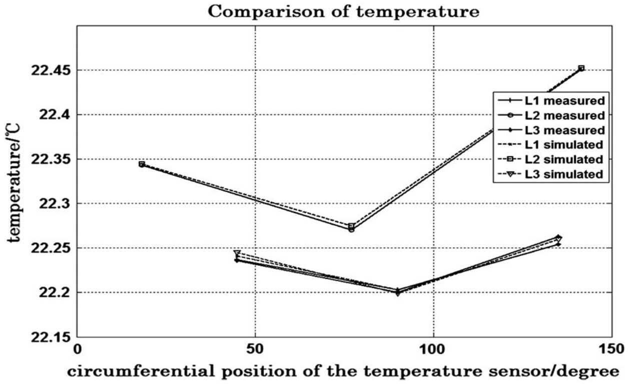

Fig. 9. Comparison of the tested and simulated temperature distribution on the three lenses.

In a further step, we measure the system's wavefront under 22°C and 24°C, respectively, by changing the temperature of the water jacket. Tested results show that, before and after temperature shift, the system's wavefront does not change, proving that uniform temperature change will not introduce asymmetric thermal aberrations for this system.

4. Impact of Structure Design on the System's Thermal Aberrations

In Section 3, we concluded that temperature gradient-induced refractive index change is the main cause of transmissive wavefront aberrations. In this section, we will study the impact of the structure's thermal dissipating capabilities and special structure configuration on the system's thermal aberrations. Now that the correctness and accuracy of the integrated optomechanical analysis method have been validated, we choose simulation method to carry out our study.

A. Impact of the Structure's Thermal Conductivity on the Systems Thermal Aberration

Four candidate metal materials of the lithographical projection lens structure that have different thermal conductivity and thermal expansion coefficient are analyzed. Table 1 lists the main physical properties of these metals.

To make a comparison, we assume the "ideal thermal dissipation condition" is that no mechanical structure thermal conduction resistance is in the system, which means the thermal contact interfaces of the three lenses is 22°C, i.e., the temperature of the lens rim is 22°C. Table 2 is the simulated rms value of the system's wavefront error and the main components of thermal aberrations.

From Table 2 we can find that, though the thermal dissipating capability of the system has been improved by choosing high thermal conductivity material, the system's thermal aberration doesnot change much. Compared with metal 304, low thermal

Table 1. Main Physical Properties of Metals

Metal Name	Density/Kg/m^3	Young's Modulus/MPa	Poisson's Ratio	Conductivity/W/m/°C	Thermal Expansion Coefficient/10^{-6}/°C
4J32	8130	148000	0.29	11.79	0.31
304	8000	193000	0.27	13.76	14.7
40Cr	7750	2060000	0.26	38.48	11.0
7075	2790	71700	0.3	117.55	23.4

Table 2. System Thermal Aberration with Different Structure Materials

		rms of Main Components of Thermal Aberration/nm			
	rms of Wavefront Error/nm	Astigmatism	Tetrad-foil	Trefoil	Hexafoil
4J32	21.65	20.78	4.56	0.47	1.45
304	21.57	20.70	4.56	0.47	1.45
40Cr	21.00	20.14	4.53	0.49	1.45
7075	20.67	19.80	4.51	0.50	1.45
Ideal condition	18.51	17.64	4.40	0.02	1.43

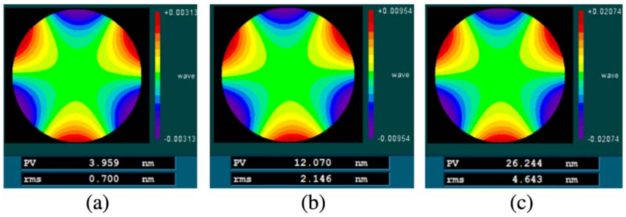

Fig. 10. Experimental verification of trefoil aberration. (a) 1 V heating voltage, (b) 2 V heating voltage, and (c) 3 V heating voltage.

expansion coefficient metal 4J32 shows no advantage. Comparing the four cases with the "ideal condition," we can conclude that the thermal dissipating capability of the structure will affect the system's thermal aberrations but won't be the decisive factor. The decisive factor is the magnitude and distribution of the heat source; on the other hand, higher thermal conductivity material will introduce fewer thermal wavefront degenerations.

B. Impact of Structure's Configuration on the System's Thermal Aberrations

The experimental system utilizes two optical element-mounting techniques: retaining ring with tangential lens-to-mount interface method and three point kinematic mounting method. Retaining the ring mounting method may introduce excessive constraints compared to the three-point kinematic mounting method. When undergoing temperature fluctuations, the former might introduce more thermal stress than the latter. Now that thermal stress is not a concern under low temperature change conditions, the uniformity of the thermal conduction should be considered. The trefoil thermal aberration component existing in the experimental and simulated results is the evidence of asymmetric contact of lens-to-mount interface induced thermal aberrations. To verify this phenomenon, we increase the heating voltage to 2 and 3 V, respectively, during the experiment to monitor the change of trefoil aberration. Figure 10 shows the results.

Along with the increasing of heating voltage, the magnitude of trefoil aberration increases, but its angle does not move, proving it dependent on the structure's thermal dissipating path, i.e., dependent on the three-point kinematic mounts.

5. Conclusions

The contribution of the three thermal effects on thermal aberrations of precision optical system caused by nonuniform heating of a laser beam is analyzed through the integrated optomechanical simulation method. The results show that temperature gradient in lens-induced change of refractive index is the main cause of thermal aberrations; the combined effect of the surface thermal deformation is only about 1/33 of that of the change of refractive index, suggesting that reduction of surface deformation is less important relative to reduction of temperature gradients when we conduct the system's structure design. And small temperature change such as 1°C will induce neglectable amount of birefringence. Experiments have been carried out to validate the correctness and accuracy of the simulation. A further study on the impact of structure design on the system's thermal aberrations shows that higher thermal conductivity material of the mounting structure will introduce less amount of additive thermal wavefront degeneration, but is not the decisive factor of thermal aberrations. Asymmetric thermal conduction of the structure's configuration will introduce mounting form dependent thermal aberrations that should be avoided. Both the simulated and tested results can provide a reference for structure design and thermal aberration analysis of the similar optical systems.

References

1. K. Mann, A. Bayer, U. Leinhos, M. Schöneck, and B. Schäfer, "Measurement of wavefront distortions in DUV optics due to lens heating," Proc. SPIE **7973**, 79732B (2011).

2. J. Zhou, Y. Zhang, P. Engblom, M. Hyatt, E. Wu, M. Snajdr, A. Devilliers, Y. He, C. Hickman, P. Liu, D. de Lang, B. Geh, E. Byers, and S. Light, “Improving aberration control with application specific optimization using computational lithography,” Proc. SPIE **7640**, 76400K (2010).
3. W. Wang, F. Tan, B. Lü, and C. Liu, “Three-dimensional calculation of high-power, annularly distributed, laser-bam-induced thermal effects on reflectors and windows,” Appl. Opt. **44**, 7442–7450 (2005).
4. J. de Klerk, C. Wagner, R. Droste, L. Levasier, L. Jorritsma, E. V. Setten, H. Kattouw, J. Jacobs, and T. Heil, “Performance of a 1.35NA ArF immersion lithography system for 40 nm applications,” Proc. SPIE **6520**, 65201Y (2007).
5. Y. Uehara, T. Matsuyama, T. Nakashima, Y. Ohmura, T. Ogata, K. Suzuki, and N. Tokuda, “Thermal aberration control for low k1 lithography,” Proc. SPIE **6520**, 65202V (2007).
6. P. R. Yoder, Jr., *Mounting Optics in Optical Instruments*, 2nd ed. (SPIE, 2008).
7. H.-S. Yang, H. Kihm, I. K. Moon, G.-J. Jung, S.-C. Choi, K.-J. Lee, H.-Y. Hwang, S.-W. Kim, and Y.-W. Lee, “Three-shell based lens barrel for the effective athermalization of an IR optical system,” Appl. Opt. **50**, 6206–6213 (2011).
8. T. Legero, T. Kessler, and U. Sterr, “Tuning the thermal expansion properties of optical reference cavities with fused silica mirrors,” J. Opt. Soc. Am. B **27**, 914–919 (2010).
9. K. I. Abdusamatov and S. I. Khankov, “Calculating the thermal aberrations of a space-based solar telescope-limbograph,” J. Opt. Technol. **73**, 24–28 (2006).
10. M. Bigelow and N. Harned, “Taking optical precision to the extreme,” oemagazine, 32–33 (2004).
11. T. Nakashima, Y. Ohmura, T. Ogata, Y. Uehara, H. Nishinaga, and T. Matsuyama, “Thermal aberration control in projection lens,” Proc. SPIE **6924**, 69241V (2008).
12. K. B. Doyle, V. L. Genberg, and G. J. Michels, *Integrated Optomechanical Analysis* (SPIE, 2002).
13. SigFit Reference Manual, version 2012R1d, Sigmadyne Inc.
14. HPFS Fused silica standard grade semiconductor optics, Corning Inc..
15. K. B. Doyle, “Thermo-elastic wavefront and polarization error analysis of a telecommunication optical circulator,” Proc. SPIE **4093**, 18–27 (2000).
16. K. B. Doyle, “Numerical methods to compute optical errors due to stress birefringence,” Proc. SPIE **4769** 34–42 (2002).
17. J. Schroeder, “Brillouin scattering and pockels coefficients in silicate glasses,” J. Non-Cryst. Solids **40**, 549–566 (1980).
18. D. Su, E. Miao, Y. Sui, and H. Yang, “Absolute surface figure testing by shift-rotation method using Zernike polynomials,” Opt. Lett. **37**, 3198–3200 (2012).